

Enhanced sensitivity and contrast with bimodal atomic force microscopy with small and ultra-small amplitudes in ambient conditions

Sergio Santos

Citation: *Applied Physics Letters* **103**, 231603 (2013); doi: 10.1063/1.4840075

View online: <http://dx.doi.org/10.1063/1.4840075>

View Table of Contents: <http://scitation.aip.org/content/aip/journal/apl/103/23?ver=pdfcov>

Published by the AIP Publishing

Instruments for advanced science

Gas Analysis



- dynamic measurement of reaction gas streams
- catalysis and thermal analysis
- molecular beam studies
- dissolved species probes
- fermentation, environmental and ecological studies

Surface Science



- UHV TPD
- SIMS
- end point detection in ion beam etch
- elemental imaging - surface mapping

Plasma Diagnostics



- plasma source characterization
- etch and deposition process
- reaction kinetic studies
- analysis of neutral and radical species

Vacuum Analysis



- partial pressure measurement and control of process gases
- reactive sputter process control
- vacuum diagnostics
- vacuum coating process monitoring

contact Hiden Analytical for further details

HIDEN
ANALYTICAL

info@hideninc.com
www.HidenAnalytical.com

CLICK to view our product catalogue



Enhanced sensitivity and contrast with bimodal atomic force microscopy with small and ultra-small amplitudes in ambient conditions

Sergio Santos

Departament de Disseny i Programació de Sistemes Electrònics, UPC-Universitat Politècnica de Catalunya Av. Bases, 61, 08242 Manresa (Barcelona), Spain

(Received 30 October 2013; accepted 19 November 2013; published online 4 December 2013)

Here, we introduce bimodal atomic force microscopy operated with sub-nm and ultra-small, i.e., sub-angstrom, first and second mode amplitudes in ambient conditions. We show how the tip can be made to oscillate in the proximity of the surface and in perpetual contact with the adsorbed water layers while the second mode amplitude and phase provide enhanced contrast and sensitivity. Nonlinear and nonmonotonic behavior of the experimental observables is discussed theoretically with a view to high resolution, enhanced contrast, and minimally invasive mapping. Fractions of meV of energy dissipation are shown to provide contrast above the noise level. © 2013 AIP Publishing LLC. [<http://dx.doi.org/10.1063/1.4840075>]

Nanoscale science and technology exploit emerging phenomena that occur when structures or domains reach the sub 100 nm range. More generally, since structure and nanoscale properties control macroscopic phenomena, over the past decades, the nanoscale has acted as a meeting point for interdisciplinary research ranging from biology to materials science.¹ A common interest relates to characterization and quantification at the nanoscale and the relationship to corresponding macroscale manifestations.² In this respect, the atomic force microscope AFM has established itself as one of the leading instruments in the field by simultaneously providing direct access to the nanoscale and enough versatility to evolve according to demand.³ For example, dynamic AFM (dAFM) modes of operation are typically employed to map the topography of conductors and insulators with nanoscale,⁴ molecular,⁵ sub-molecular,^{6–9} and sometimes atomic resolution.^{10–12} These dynamic modes typically provide alternative channels¹³ to simultaneously map compositional variations.¹⁴ The scientific community is in fact actively seeking to increase the number¹⁵ and sensitivity¹³ of contrast channels^{12,16,17} since these can be employed to quantify^{18,19} nanoscale properties and enhance resolution and/or contrast.^{12,20,21}

Recently, two groups^{8,11} have independently reported that the tip of the AFM can be made to oscillate with sub-nm amplitudes, and in the proximity of the surface, i.e., near or in the mechanical contact region, while enhancing resolution even in the presence of adsorbed water layers in ambient conditions. Here, we introduce bimodal AFM, where the second flexural mode of the cantilever is excited with ultra-small oscillation amplitudes while oscillating under such conditions. While the results could be extended to the dual frequency modulation (FM-FM) mode, here, the discussion focuses on bimodal amplitude modulation (AM) AFM. That is, the feedback is assumed to operate on the amplitude of the first flexural mode and the second amplitude and phase are left open loop to sense and enhance compositional contrast. Nonlinear and nonmonotonic behavior of the experimental observables is discussed theoretically by numerically integrating the equation of motion, with a

view to high resolution, enhanced contrast and minimally invasive mapping.

The first aim here is to operate under the imaging conditions illustrated in Fig. 1 (and reported in Refs. 8 and 11) since these have been shown to be optimum conditions for high resolution imaging in several studies.^{11,22} These imaging conditions, or region, are here termed Small Amplitude Small Set-point⁸ (SASS) conditions. Then, a second external drive is added to the second mode to enhance contrast^{12,13,23} and possibly resolution and quantification.²⁴ The interaction of the nanoscopic tip is magnified in the illustration (top) in order to emphasize that the oscillation amplitudes of both the first and the second modes are of the same order of magnitude, or even smaller, than molecular bonds. The motivation is to force the tip to oscillate under, and the dynamics of the cantilever to be controlled by, the influence of localized surface forces only. Note also that when adsorbed water layers are present, the tip should oscillate in perpetual contact with these layers^{8,25} and as close as possible to the surface¹¹ while minimizing sample deformation. These are the SASS conditions and have been recently reported^{8,11} to decrease background noise and enhance stability and resolution. The flexural modes of the cantilever are modeled with the standard equations¹³

$$\frac{k_m}{\omega_m^2} \ddot{z}_m(t) + \frac{k_m}{Q_m \omega_m} \dot{z}_m(t) + k_m z_m = F_{01} \cos(\omega_1 t) + F_{02} \cos(\omega_2 t) + F_{ts}, \quad (1)$$

where the subscript m (here, m = 1, 2 only for simplicity) stands for mode, F_{01} and F_{02} are the magnitudes of the two external driving forces at frequencies ω_1 and ω_2 , respectively, F_{ts} is the tip-sample interaction and k_m , ω_m , and Q_m are the modal stiffness, resonance frequency, and Q factor. Here, the (free) resonance frequencies coincide exactly with the drive frequencies for simplicity and the subscripts stand for first and second modes. The instantaneous tip position z when interacting is

$$z(t) = A_1 \cos(\omega_1 t - \phi_1) + A_2 \cos(\omega_2 t - \phi_2) + O(\varepsilon), \quad (2)$$

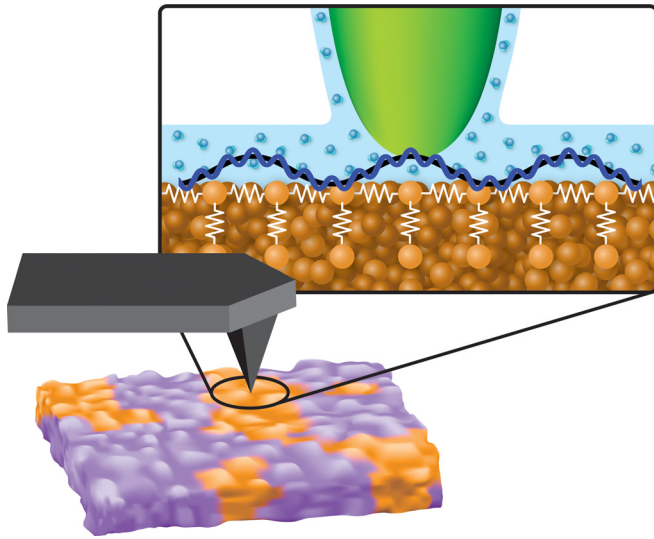


FIG. 1. Scheme of an atomic force microscope (AFM) cantilever illustrating how bimodal AFM can be made to operate with small and ultra-small amplitudes in the proximity of the surface while the tip oscillates in perpetual contact with the adsorbed water layer.

where A_1 , A_2 , ϕ_1 , and ϕ_2 are the oscillation amplitudes and phase shifts at ω_1 and ω_2 , respectively, and $O(\varepsilon)$ stands for the higher harmonic contributions which can be typically neglected. Here, in the long range, F_{ts} is defined by the Hamaker constant H

$$F_{ts}(d) = -\frac{RH}{6(d-h)^2} \quad h + a_0 < d, \quad (3)$$

where d is the tip-sample distance, R is the tip radius, h is the height of the water layer,²⁵ and a_0 is an intermolecular distance (here, $h = 1$ nm and $a_0 = 0.165$ nm throughout). Inside the water layer ($a_0 < d < h + a_0$) F_{ts} is assumed to be constant

$$F_{ts} \equiv F_{AD} = -\frac{RH}{6a_0^2} \quad a_0 < d \leq h + a_0. \quad (4)$$

Finally, when mechanical contact occurs, the Derjaguin Muller Toporov (DMT) model of contact mechanics²⁶ gives

$$F_{DMT}(d) = -\frac{RH}{6a_0^2} + \frac{4}{3}E^*\sqrt{R}\delta^{3/2} \quad a_0 \leq d, \quad (5)$$

where E^* is the effective Young Modulus and δ is the tip-sample deformation ($\delta = a_0 - d$). This model is conservative, consistent with force profiles in ambient conditions,^{27,28} and H and E^* define chemical and mechanical properties, respectively. The parameters employed in this work (unless otherwise stated) are: $k_1, k_2 = 40$ and 1600 N/m, $f_1 = 300$ kHz ($\omega = 2\pi f$), $f_2 = 1.8$ MHz, $Q_1 = 450$, $Q_2 = 2700$, $A_{01} \equiv A_0 = 3$ nm (free amplitude at ω_1), $A_{02} = 0$ for monomodal or mm and 50 pm for bimodal or bim operation (free amplitude at ω_2), $E_t = 120$ GPa (tip), $E_s = 1$ GPa (sample), $H = 4.1 \times 10^{-20}$ J, and $R = 3$ nm. Note that the modal frequencies have been assumed to be integer multiples of each other. Experimentally this might or might not be the case^{16,22,29} but it does not affect the discussion here. Macrons imply normalized parameters throughout.

The results of numerically (fourth order Runge Kutta algorithm) integrating (1) with the force profile that (3) to (5) define are shown in Fig. 2. First, the normalized oscillation amplitude \bar{A}_1 ($\bar{A}_1 = A_1/A_0$) is plotted in terms of cantilever sample separation z_c (Fig. 2(a)) and minimum distance of approach d_m or simply d , i.e., $\bar{A}_1(d)$ (Fig. 2(b)). Note the positive slope in \bar{A}_1 where $z_c \approx 0$ nm in Fig. 2(a). This is the SASS region⁸ and it is highlighted with dashed circles in Fig. 2 throughout. The other region of positive slope in \bar{A}_1 in Fig. 2(a) coincides with the standard attractive regime (AR) of operation or attractive \bar{A}_1 branch.³⁰ These are the only two regions available for imaging when employing sufficiently small values of A_0 since the other region, i.e., the one with a negative slope in \bar{A}_1 , is not suitable for AM operation. The normalized force $\bar{F}_{ts} = F_{ts}/|F_{AD}|$ (dashed lines) is also plotted in Fig. 2(b). First, from Fig. 2(b), it can be concluded that the tip oscillates high above the sample's surface, and only gently and intermittently senses the water layer, i.e., $d > h$, in the standard AR regime. Second, when the tip interacts with the water layer in the flat \bar{F}_{ts} region, i.e., $a_0 < d < h + a_0$, \bar{A}_1 increases with decreasing z_c (Fig. 2(a)) giving rise to the negative slope region in \bar{A}_1 . Third, for smaller separations (Fig. 2(a)), i.e., $z_c \approx 0$ nm, and distances (Fig. 2(b)), i.e., $d < a_0$, a second region of positive slope in \bar{A}_1 is found, i.e., the SASS region. At this point (1) the cantilever oscillates with small amplitudes, i.e., sub-nm, and (2) the tip is always under the water layer, i.e., $d < h + a_0$ throughout (Fig. 2(b)), as illustrated in Fig. 1. The SASS region thus accomplishes the first objective of this work, i.e., oscillating under the influence of localized surface forces only. Also note that, even though the point of mechanical contact cannot be directly established experimentally, $\bar{A}_1(d)$ can be potentially plotted from experimental amplitude curves by employing the approximation $d \approx z_c - A_1$ since both z_c and A_1 are experimental observables. This would lead to experimental $\bar{A}_1(d)$ curves⁸ such as that shown in Fig. 2(b). In Figs. 2(c) and 2(d), the second mode amplitude, i.e., $\bar{A}_2 = A_2/A_{02}$, is plotted in terms of z_c and d , respectively, when (1) $A_{02} = 0$ pm (monomodal or mm operation) and (2) $A_{02} = 50$ pm (bimodal or bim operation); circles and blue

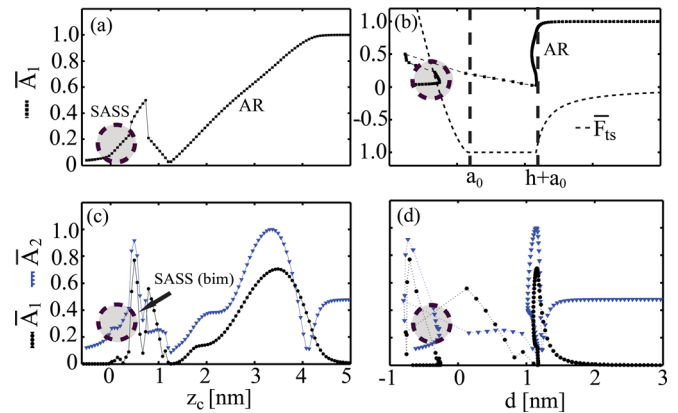


FIG. 2. Simulations of monomodal (mm) and bimodal (bim) AFM. Normalized fundamental amplitude \bar{A}_1 as a function of (a) cantilever separation z_c and (b) tip-sample distance d . The tip-sample force is also shown in (b) with dashed lines. Normalized second mode amplitude \bar{A}_2 as a function of (c) separation z_c and (d) tip-sample distance d under monomodal mm (circles) and bimodal bim (blue triangles) operation.

TABLE I. Numerical values of some of the relevant physical and dynamic parameters and their variations with increasing Young Modulus of the sample E_s in bimodal AFM operated under SASS conditions.

E_s [GPa]	d_m [pm]	Δd_m^* [pm]	Δd_m [pm]	F_p [pN]	ΔF_p [pN]	ϕ_1 [°]	$\Delta\phi_1$ [°]	ϕ_2 [°]	$\Delta\phi_2$ [°]	A_2 [pm]	ΔA_2 [pm]
1	-283.8	28.6	0.0	2.8	0.0	3.80	0.0	24.73	0.0	20.9	0.0
2	-122.3	29.6	161.5	14.9	12.1	3.69	-0.10	25.02	0.29	19.8	-1.2
10	34.1	29.9	317.9	356.0	353.2	4.85	1.05	175.20	150.47	14.5	-6.4
100	119.8	15.7	403.7	574.6	571.8	2.68	-1.13	70.63	45.90	7.4	-13.5

triangles, respectively. Also, A_2 is normalized with 50 pm throughout even when $A_{02} = 0$ pm. At this point, it should be noted that in the simulations the behavior of \bar{A}_1 was not altered during bimodal operation. The nonmonotonic behavior of \bar{A}_2 with decreasing z_c is obvious from Fig. 2(c). To a first approximation,³¹ the noise level should be ≈ 10 pm ($k_1 = 40$ N/m) and ≈ 1 pm ($k_2 = 1600$ N/m) for the first and second modes, respectively. The data in Figs. 2(c) and 2(d) further indicate that in the SASS region the values of \bar{A}_2 remain above 10 pm, i.e., above the noise level, only when the second mode is externally excited, i.e., bimodal operation. Under monomodal operation $\bar{A}_2 > 0$ pm because of the non-linear force F_{ts} . The capacity of enhancing and mapping compositional contrast via variations in \bar{A}_2 and ϕ_2 even for relatively stiff cantilevers, i.e., $k_1 = 40$ N/m, is discussed next.

First, a set of sample's Young Modulus has been employed in the simulations $E_s = 1, 2, 10$, and 100 GPa during bimodal operation as shown in Table I. Here, the set-point was set to $A_1 = 200$ pm, the SASS region was reached and A_2 and ϕ_2 were left open loop. For the different values of E_s , the table shows: minimum distance of approach d_m , error $\Delta d_m^* = (z_c - A_1) - d_m$, variations Δd_m (always with increasing E_s and relative to the value for 1 GPa), peak force F_p or $F_{ts}(d_m)$ and variations ΔF_p , ϕ_1 and variations $\Delta\phi_1$, ϕ_2 and variations $\Delta\phi_2$, A_2 and variations ΔA_2 . The experimental observables leading to compositional contrast maps (relative to $E_s = 1$ GPa in Table I) are $\Delta\phi_1$, $\Delta\phi_2$, and ΔA_2 . First note that even conservative interactions alone might lead to standard phase shift $\Delta\phi_1$ contrast above the noise level,³² i.e., $\sim 0.1^\circ$, in bimodal AFM when operating under SASS conditions. This can be attributed to harmonic distortion (HD)³³ since, from the table, $A_2/A_1 \sim 0.1$. Furthermore, for $E_s = 100$ GPa, other higher harmonics reached amplitudes in the order of pm (not shown). Second, $\Delta\phi_1$ behaves nonmonotonically with variations in E_s . Nonmonotonic behavior in $\Delta\phi_1$ with for large values of HD in liquid environments³³ and a variety of regimes of operation in bimodal AFM¹⁵ have been recently reported. Third, $\Delta\phi_2$ takes values up to

an order of magnitude larger than $\Delta\phi_1$ implying that conservative compositional variations can be mapped with higher contrast via $\Delta\phi_2$. Again $\Delta\phi_2$ varies nonmonotonically with E_s . Third, ΔA_2 can take values larger than ten pm implying that these are in principle also detectable experimentally. Moreover, the behavior of ΔA_2 is monotonic with E_s for the range in the table. Finally, it is worth mentioning that by employing $A_0 = 10$ nm and $A_1 = 7$ nm in the simulations (standard repulsive imaging conditions not shown here) for $E_s = 1$ GPa, the tip-sample deformation $\delta = a_0 - d_m$ reached 1.57 nm as opposed to the 0.45 nm in SASS.

Next, Table II shows the results in bimodal AFM operated under SASS conditions with variations in viscosity $\eta = 0, 1, 10, 100$, and 1000 Pa \times s rather than E_s . The dissipative force³³ is

$$F_{dis}(\delta) = -\eta(R\dot{\delta})^{1/2} \times \dot{\delta} \quad \delta > 0. \quad (6)$$

First note from Table II that both $\Delta\phi_1$ and $\Delta\phi_2$ monotonically increase with viscosity η . In particular, even variations of 1 Pa \times s can produce variations $\Delta\phi_2$ larger than 0.1° . Second, the contrast due to $\Delta\phi_2$ can be up to a factor of 4 or 5 larger than that due to $\Delta\phi_1$. Third, A_2 monotonically decreases with increasing η and variations ΔA_2 can be larger than 10 pm.

In standard monomodal AM AFM imaging, the energy dissipated per cycle $E_{dis}(1)$ (at resonance) is computed as^{24,34}

$$E_{dis}(1) = \frac{\pi k_1 A_0 A_1}{Q_1} \left[\sin(\phi_1) - \frac{A_1}{A_0} \right]. \quad (7)$$

The above expression accounts for the fundamental frequency ω_1 and mode only. In bimodal AFM, the contribution to E_{dis} from the second modal frequency ω_2 can be computed as

$$E_{dis}(2) = \frac{n\pi k_2 A_{02} A_2}{Q_2} \left[\sin(\phi_2) - \frac{A_2}{A_{02}} \right], \quad (8)$$

TABLE II. Numerical values of some of the relevant physical and dynamic parameters and their variations with increasing viscosity η in bimodal AFM operated under SASS conditions.

η [Pa \times s]	d_m [pm]	Δd_m^* [pm]	Δd_m [pm]	F_p [pN]	ΔF_p [pN]	ϕ_1 [°]	$\Delta\phi_1$ [°]	ϕ_2 [°]	$\Delta\phi_2$ [°]	A_2 [pm]	ΔA_2 [pm]
0	-283.8	28.6	0.0	2.8	0.0	3.80	0.0	24.73	0.0	20.9	0.0
1	-283.7	28.6	0.1	2.6	-0.2	3.86	0.06	25.06	0.33	20.9	0.0
10	-283.0	28.2	0.8	0.8	-2.0	4.46	0.66	27.94	3.21	20.4	-0.6
100	-274.2	25.1	9.6	-21.4	-24.2	10.30	6.50	49.03	24.3	15.3	-5.7
1000	-143.8	25.1	140.0	-322.0	-324.8	51.60	47.80	93.20	68.47	4.0	-17.0

TABLE III. Energy dissipation analysis corresponding to the conditions in Table II and in bimodal AFM operated under SASS conditions. Energy units are meV.

η [Pa \times s]	E_{dis}	$E_{\text{dis}}(1)$	$\Delta E_{\text{dis}}(1)$	$E_{\text{dis}}(2)$	$E_{\text{dis}}(1,2)$	$\Delta E_{\text{dis}}(1,2)$
0	0.0	-0.4	-0.4	0.0	-0.5	-0.5
1	0.9	0.75	-0.2	0.4	1.2	0.2
10	15.8	11.6	-4.2	4.3	15.9	0.1
100	140.9	117.3	-23.6	23.9	141.2	0.3
1000	762.5	749.7	-12.8	12.7	762.4	-0.1

where here $n=6$ since $\omega_2=6\omega_1$. Then, the total energy dissipated per cycle E_{dis} can be approximated as $E_{\text{dis}} \approx E_{\text{dis}}(1) + E_{\text{dis}}(2)$. In the simulations, E_{dis} has been calculated numerically as the work done by F_{ts} per cycle. Numerical errors were in the order of fractions of meV or less. Table III shows (for the values of η in Table II): E_{dis} , $E_{\text{dis}}(1)$, the error $\Delta E_{\text{dis}}(1) = E_{\text{dis}}(1) - E_{\text{dis}}$, $E_{\text{dis}}(2)$, $E_{\text{dis}}(1,2) = E_{\text{dis}}(1) + E_{\text{dis}}(2)$, and the error $\Delta E_{\text{dis}}(1,2) = E_{\text{dis}}(1,2) - E_{\text{dis}}$. Energy units are meV throughout. First note that E_{dis} in SASS stays always below 1 eV even when η is largest, i.e., $\eta = 10^3$ Pa·s, in agreement⁸ with the literature. Second, errors of only tens of meV can follow from ignoring the contribution from $E_{\text{dis}}(2)$ in SASS. This would not be the case in standard repulsive imaging. For example, in the repulsive imaging conditions above and for $\eta = 10$ Pa \times s, $E_{\text{dis}} = 1.6$ eV, $E_{\text{dis}}(1) = 5.7$ eV, $E_{\text{dis}}(2) = -4.1$ eV, and $E_{\text{dis}}(1,2) = 1.6$ eV. This implies that $E_{\text{dis}}(2)$ can be negative and should not be ignored in repulsive bimodal imaging. The data in Tables II and III further indicate that dissipation in the order of 1–10 meV should be readily detectable (~ 0.1 – 1°) via $\Delta\phi_2$ under bimodal SASS operation. In particular, Table III shows that E_{dis} below a single meV ($\eta = 1$ Pa \times s) can lead to fractions of degrees of contrast $\Delta\phi_2$. These energies are at least one order of magnitude smaller than those due to a single van der Waals bond and indicate that, in principle, bimodal SASS could be made to operate in the energy dissipation mode with energies in the order of 1–10 meV. In summary, a way to operate bimodal AFM with small and ultra-small first and second mode amplitudes, and in close proximity to the surface, has been shown to lead to enhanced contrast and sensitivity for mapping conservative and dissipative nanoscale heterogeneity.

- ¹R. M. Brydson, C. Hammond, D. Mowbray, M. R. J. Gibbs, I. Todd, M. Grell, I. W. Hamley, M. Geoghegan, R. A. L. Jones, and G. J. Leggett, *Nanoscale Science and Technology* (Wiley, Chichester, 2005).
- ²H. Assender, V. Bliznyuk, and K. Porfyrakis, *Science* **297**, 973–976 (2002).
- ³M. Lucas and E. Riedo, *Rev. Sci. Instrum.* **83**, 061101 (2012).
- ⁴O. Kolosov, A. Gruverman, J. Hatano, K. Takahashi, and H. Tokumoto, *Phys. Rev. Lett.* **74**, 4309–4312 (1995).
- ⁵T. Fukuma, K. Kobayashi, K. Matsushige, and H. Yamada, *Appl. Phys. Lett.* **86**, 193108–193110 (2005).
- ⁶N. H. Thomson, *Ultramicroscopy* **105**, 103–110 (2005).
- ⁷A. San Paulo and R. Garcia, *Biophys. J.* **78**, 1599–1605 (2000).
- ⁸S. Santos, V. Barcons, H. K. Christenson, D. J. Billingsley, W. A. Bonass, J. Font, and N. H. Thomson, *Appl. Phys. Lett.* **103**, 063702–063705 (2013).
- ⁹A. Cerreta, D. Vobornik, and G. Dietler, *Eur. Polym. J.* **49**, 1916–1922 (2013).
- ¹⁰F. J. Giessibl, *Science* **267**, 68–71 (1995).
- ¹¹D. S. Wastl, A. J. Weymouth, and F. J. Giessibl, *Phys. Rev. B* **87**, 245415–245424 (2013).
- ¹²S. Kawai, T. Glatzel, S. Koch, B. Such, A. Baratoff, and E. Meyer, *Phys. Rev. Lett.* **103**, 220801–220804 (2009).
- ¹³T. Rodriguez and R. Garcia, *Appl. Phys. Lett.* **84**(3), 449–551 (2004).
- ¹⁴R. Garcia, R. Magelele, and R. Perez, *Nature Mater.* **6**, 405–411 (2007).
- ¹⁵D. Kiracofe, A. Raman, and D. Yablon, *Beilstein J. Nanotechnol.* **4**, 385–393 (2013).
- ¹⁶R. Garcia and E. T. Herruzo, *Nat. Nanotechnol.* **7**, 217–226 (2012).
- ¹⁷A. Raman, S. Trigueros, A. Cartagena, A. P. Z. Stevenson, M. Susilo, E. Nauman, and S. A. Contera, *Nat. Nanotechnol.* **6**, 809–814 (2011).
- ¹⁸E. T. Herruzo and R. Garcia, *Beilstein J. Nanotechnol.* **3**, 198–206 (2012).
- ¹⁹D. Platz, D. Forchheimer, E. A. Tholén, and D. B. Haviland, *Nat. Commun.* **4**, 1360 (2013).
- ²⁰R. Proksch, *Appl. Phys. Lett.* **89**, 113121–113123 (2006).
- ²¹G. Chawla and S. D. Solares, *Appl. Phys. Lett.* **99**, 074103 (2011).
- ²²O. Sahin, C. Quate, O. Solgaard, and F. J. Giessibl, in *Springer Handbook of Nanotechnology*, edited by B. Bhushan (Springer-Berlin-Heidelberg, 2007).
- ²³S. Kawai, T. Glatzel, S. Koch, B. Such, A. Baratoff, and E. Meyer, *Phys. Rev. B* **81**, 085420–085426 (2010).
- ²⁴J. R. Lozano and R. Garcia, *Phys. Rev. B* **79**, 014110–014118 (2009).
- ²⁵S. Santos, A. Verdager, T. Souier, N. H. Thomson, and M. Chiesa, *Nanotechnology* **22**(46), 465705–465713 (2011).
- ²⁶B. V. Derjaguin, V. Muller, and Y. Toporov, *J. Colloid Interface Sci.* **53**(2), 314–326 (1975).
- ²⁷C. A. Amadei, S. Santos, S. O. Pehkonen, A. Verdager, and M. Chiesa, *J. Phys. Chem. C* **117**, 20819–20825 (2013).
- ²⁸S. Leroy and M. Wendland, *Langmuir* **29**(40), 12410 (2013).
- ²⁹O. Sahin, C. Quate, O. Solgaard, and A. Atalar, *Phys. Rev. B* **69**(16), 165416 (2004).
- ³⁰R. Garcia and A. San Paulo, *Phys. Rev. B* **60**(7), 4961–4967 (1999).
- ³¹H.-J. Butt and M. Jaschke, *Nanotechnology* **6**, 1–7 (1995).
- ³²J. R. Lozano and R. Garcia, *Phys. Rev. Lett.* **100**, 076102–076105 (2008).
- ³³A. F. Payam, J. R. Ramos, and R. Garcia, *ACS Nano* **6**(6), 4663–4670 (2012).
- ³⁴J. P. Cleveland, B. Anczykowski, A. E. Schmid, and V. B. Elings, *Appl. Phys. Lett.* **72**(20), 2613–2615 (1998).